13 Evaluation of Malignant Bone Disease Using DW-MRI

K. Nakanishi and A. Gutzeit

CONTENTS

SUMMARY

The bones are frequently involved as a site of metastatic disease in patients with cancer. Accurate determination of the presence, location and extent of bone involvement is of therapeutic and prognostic importance. Diffusion-weighted MR imaging performed regionally or as whole-body imaging has been shown to have a high diagnostic accuracy for the identification of bone metastases when combined with conventional MR imaging. Both qualitative and quantitative DW-MRI have also been found to be of value for distinguishing between benign and malignant causes of vertebral fractures. There is also promise in the application of quantitative ADC for evaluating treatment response of malignant bone diseases, as current imaging criteria are inadequate in assessing treatment changes of bone lesions to therapy.

K. Nakanishi, MD, PhD
Department of Diagnostic Radiology, Osaka Medical Center for Cancer and Cardiovascular Diseases, Nakamichi, Higashinari-Ku, 537-8511 Osaka, Japan
A. Gutzeit, MD
Department of Diagnostic and Interventional Radiology, Kantonsspital Winterthur, Brauerstrasse 15, Postfach 834, CH-8401 Winterthur, Switzerland

13.1 Introduction

DW-MRI is widely used for imaging of the central nervous system, especially for the diagnosis of acute stroke, although its use in the body has been

limited because of several artefacts due to cardiac motion, respiration and limited signal-to-noise ratio (Ichikawa and Araki 1999; Guo et al. 2002; Huisman 2003; Takahara et al. 2004). However, advances in MR imaging technologies have enabled reliable acquisition of DW-MR images in the body using relatively high *b*-values (e.g. $b = 1{,}000\,s/mm^2$) (Ichikawa and Araki 1999). By applying the diffusion-weighted whole-body imaging with background signal suppression (DWIBS) technique, whole-body DW-MR images can be acquired within a reasonable scan time for disease evaluation. When these images are displayed using an inverted grey scale, they superficially resemble images acquired using 18-fluorodeoxyglucose positron emission tomography (PET) imaging (Takahara et al. 2004) and have been shown to be helpful for tumour assessment (see Chap. 14).

MR imaging results in intrinsically high image contrast between soft tissues and bones (Sugimoto et al. 1988; Jacobsson et al. 1991; Imamura et al. 2000; Nakanishi et al. 2005, 2007). With increasing age, the normal cellular marrow is replaced by fat, thus modifying the signal characteriztics of the bone marrow on MR imaging. However, the fat-replaced bone marrow provides a high signal intensity background to facilitate the detection of hypointense disease on conventional T1-weighted MR imaging. There is also emerging data that support the use of DW-MRI (Nonomura et al. 2001) for the detection and characterization of bone involvement in patients with cancer, as well as for assessing tumour response to treatment. The evaluation of tumour response to treatment of bone disease is particularly challenging because to date, there is no reliable imaging technique that can be applied to quantify the degree of treatment change. As emphasized in previous chapters, assessment of bone disease should not be made in isolation using DW-MRI, but should be combined with conventional imaging (including radiographs, CT and conventional MR imaging) for the best assessment to be made.

In this chapter, we will survey the range of malignant conditions that may be encountered in the bones of oncological patients. Conventional and DW-MRI imaging techniques that can be applied for the detection and characterization of bone involvement will be discussed. The emphasis of discussion will be on the evaluation of metastatic bone disease and in the systemic workup of patients with underlying cancer to determine the extent of disease involvement. We will also survey the imaging criteria that have been developed for the assessment of tumour response to treatment in bones, and highlight the potential of DW-MRI as an imaging technique that can be used to monitor treatment change. Last but not least, we will review some benign bone conditions, which may mimic malignant bone diseases on DW-MRI.

13.2 Malignant Conditions of the Bones

Bone tumours can generally be divided into two groups: benign and malignant bone tumours. Malignant bone tumours can in turn be subdivided into primary malignant bone tumours and bone metastases.

When a focal bone lesion is encountered, knowledge of the age of the patient and the location of disease are helpful for image interpretation. Imaging features which are useful for lesion characterization include the nature of the tumour matrix, the zone of transition of the lesion and adjacent bone or soft tissue changes. One of the key features in radiological assessment is identifying the presence and nature of any associated periosteal reaction, which may be characterized as interrupted or non-interrupted, the former being typical of malignant bone diseases. When all these factors are considered, it is possible in most cases to make a relatively specific radiological diagnosis before definitive histological confirmation becomes available (Miller 2008).

Bone metastases are the most common malignant bone tumours and for this reason should always be considered in the differential diagnoses of suspicious lesions, especially in the elderly. In patients with cancer, the development of metastatic bone involvement represents disseminated disease which carries a poor prognosis. As such, accurate determination of the presence and extent of bone metastases is important. Bone metastases commonly arise from tumours of the lung, breast, prostate and thyroid, and usually affect vertebrae of the spine, skull and proximal long bones. Not uncommonly, bone metastases may be complicated by a pathological fracture, which may make it difficult to identify the malignant disease in the presence of substantial secondary changes. The bones can also be affected by haematological malignancies including lymphomas. Leukaemia and multiple myeloma frequently infiltrate the bone marrow, and involvement may be focal or diffuse (Baur-Melnyk et al. 2008a, b). Non-invasive imaging techniques are

viewed upon as important tools to assess prognosis of the disease and for planning treatment strategies in patients with haematological malignancies (Lecouvet 1998). However, the lack of existing standards for assessing bone involvement in malignant bone disease remains an unresolved radiological issue.

13.3 Conventional Imaging for the Detection of Bone Involvement in Cancer

In clinical practice, the first step taken to diagnose bone disease is usually by conventional radiography. The main disadvantage of this technique is the low sensitivity. Bone metastasis is only visible at the earliest when there has been a loss of the bone mineral content of 50% or more (Rubens 1998) (Fig. 13.1). For this reason, additional imaging such as CT, radionuclide bone scans, ^{18}FDG-PET or MR imaging are frequently employed.

CT is highly sensitive for identifying cortical destruction, pathological fractures, and periosteal changes. Other advantages of CT include its wide availability and quick examination time. By performing high-resolution imaging, it is possible to perform 3D and multiplanar image reconstructions to provide the surgeon with spatially relevant information for surgical planning. However, the main drawbacks of CT are its low sensitivity for small volume disease affecting the bones and the relatively high radiation exposure (Mahner et al. 2008).

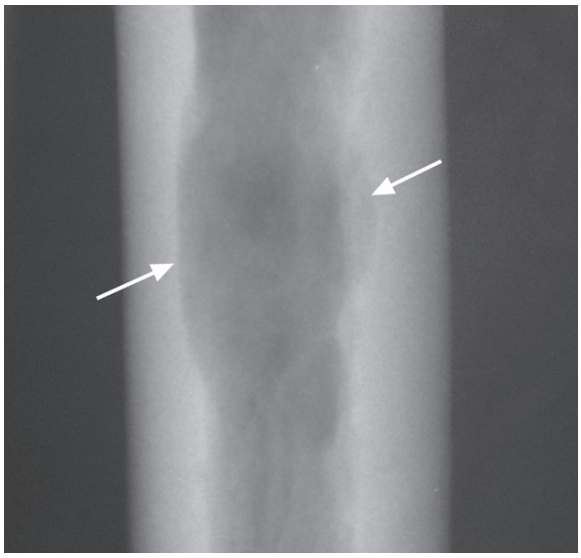

Fig. 13.1. Magnified view of the mid right humerus of a 68-year-old man with multiple myeloma shows endosteal scalloping of the inner bony cortex due to myelomatous disease infiltration (*arrows*). However, the radiograph is relatively insensitive to pathological processes and the radiograph may be normal even in the presence of significant disease infiltration

The sensitivity of radionuclide bone scintigraphy is dependent on the osteoblastic activity associated with the pathological process. The technique is very sensitive for bone metastases, especially for osteoblastic disease arising from breast and prostate cancers (Hricak et al. 2007). The key disadvantage is its lower sensitivity for lytic bone disease (e.g. metastases from renal cell and bladder carcinoma) and bone marrow infiltration (e.g. leukaemia and multiple myeloma). For example, the sensitivity of bone scintigraphy for detecting myeloma deposits is only 40–60%, this being the reason that the technique is not used for routine disease staging (Winterbottom et al. 2009). A further limitation of bone scintigraphy is the potential false-positives that can arise from healing fractures or degenerative changes.

^{18}FDG-PET is more sensitive than bone scan for detecting bone malignancies because tumours show higher tracer uptake as a result of increased metabolism (Cheran et al. 2004). Although ^{18}FDG-PET is more specific, issues remain with regards to small lesions (<1 cm), radiation burden with repeated scans and poor visualization of tumours with low metabolic activity (e.g. prostate carcinoma, renal cell carcinoma, bronchoalveolar cell carcinoma).

MR imaging has been shown to be a highly sensitive technique for the detection of bone diseases, such as bone metastases. Conventional MR imaging includes T1-weighted, T2-weighted and STIR imaging as well as contrast-enhanced T1-weighted sequences. Specialized imaging protocols combining these techniques have been used with reportedly good results. With the introduction of whole-body MR imaging using multi-channel receiver coils, this has enabled imaging of the body from head to toe. Whole-body MR imaging has been adopted for the evaluation of bone and bone marrow diseases and several studies have confirmed that the diagnostic accuracy using MR imaging is higher than radionuclide bone scintigraphy and CT for the detection of bone metastases and primary tumours (Eustace et al. 1997; Costelloe et al. 2009).

13.4 Considerations for Conventional MR Imaging and DW-MRI

Diffusion-weighted MR imaging is a promising new tool for the detection and evaluation of malignant bone diseases. However, the technique should not be used in isolation. High-quality morphological imaging (especially T1-weighted imaging) is also necessary to aid interpretation of observed changes within the bones and for precise anatomical localization of the lesion. To date, there have been few larger-scale studies comparing the diagnostic accuracy of DW-MRI alone or in combination with conventional morphological imaging for the assessment of malignant bone diseases. It will be important that further studies are undertaken in the future.

13.4.1 Conventional MR Imaging

When using conventional MR imaging to assess bone disease, evaluation is usually made using T1-weighted and short-tau inversion recovery (STIR) imaging. This combination of sequences has been shown to be effective for the detection of focal bone diseases (Yasumoto et al. 2002; Schmidt et al. 2009). Imaging should be performed in two orthogonal planes to provide accurate information on the exact anatomical localization and extension of the lesion. Compared with DW-MRI, conventional T1-weighted and STIR images are usually acquired at higher spatial resolution, which provides better anatomical delineation of disease. In particular, T1-weighted imaging is useful for identifying foci of sclerotic bone disease, as these lesions are relatively signal suppressed on STIR and high *b*-value DW-MR imaging. Thus, combining T1-weighted imaging with STIR and DW-MR imaging can be helpful towards evaluating the osteolytic vs. osteosclerotic disease fractions, thereby providing useful information which may reflect on the underlying tumour biology.

Conventional T1-weighted and STIR imaging can be incorporated into a whole-body imaging protocol for disease assessment. This is typically achieved by performing T1-weighted fast spin-echo (SE) and STIR imaging in the sagittal and coronal planes at multiple anatomical stations in the body. Such imaging implementation is well described in the published literature (Eustace et al. 1997; Schmidt et al. 2009). One suggested imaging protocol is outlined below:

- *T1-weighted sagittal images of the spine*. Five image sections of T1-weighted fast spin-echo images of the spine are acquired in the sagittal plane using three imaging stations [TR/TE, 400/13 ms. Echo train length (ETL) 4, section thickness 7, 300 mm field of view (FOV), scan matrix = 352 × 264, imaging time 4 min 33 s].
- *T1-weighted coronal images of the whole body*. 32 fast spin-echo T1-weighted images of the whole body acquired coronally using six imaging stations [TR/TE100/4.6 ms, ETL 128, 7 mm section thickness, 300 mm FOV, scan matrix = 240 × 180, imaging time 6 min 24 s].
- *STIR sagittal images of the spine*. Five STIR sagittal image sections of the whole spine acquired using three imaging stations [TR/TE/TI 2,500/70/170 ms, ETL 15, section thickness 7, 300 mm FOV, scan matrix 288 × 316, imaging time 6 min 15 s].
- *STIR coronal images of whole body*. 32 STIR images of the whole body acquired coronally at six imaging stations [TR/TE/TI 1,350/40/165 ms, ETL 65, section thickness 7, 300 mm FOV, scan matrix = 320 × 185, imaging time 6 min 24 s].

With technological advancement, it is now possible to perform high spatial resolution T1-weighted imaging using a 3D volume interpolated technique (Thomson et al. 2008). One variant of this approach is to apply a fat–water separation sequence, such as one employing a 2-point DIXON technique, which would enable fat-only and water-only images to be generated. The water-only images resemble fat-suppressed images and can be helpful for lesion identification (Suarez et al. 2009; Vanel et al. 2009) (Fig. 13.2). 3D volume interpolated imaging may also be acquired before and after contrast administration (Thomson et al. 2008).

13.4.2 Diffusion-Weighted MR Imaging (DW-MRI)

13.4.2.1 Regional DW-MRI

DW-MRI is usually performed in the body across a target region of interest using a free-breathing single-shot echo-planar imaging technique. Imaging is typically performed in the axial plane. The choice and number of *b*-values included in the measurement depends in part on whether the images are to be used for qualitative or quantitative assessment.

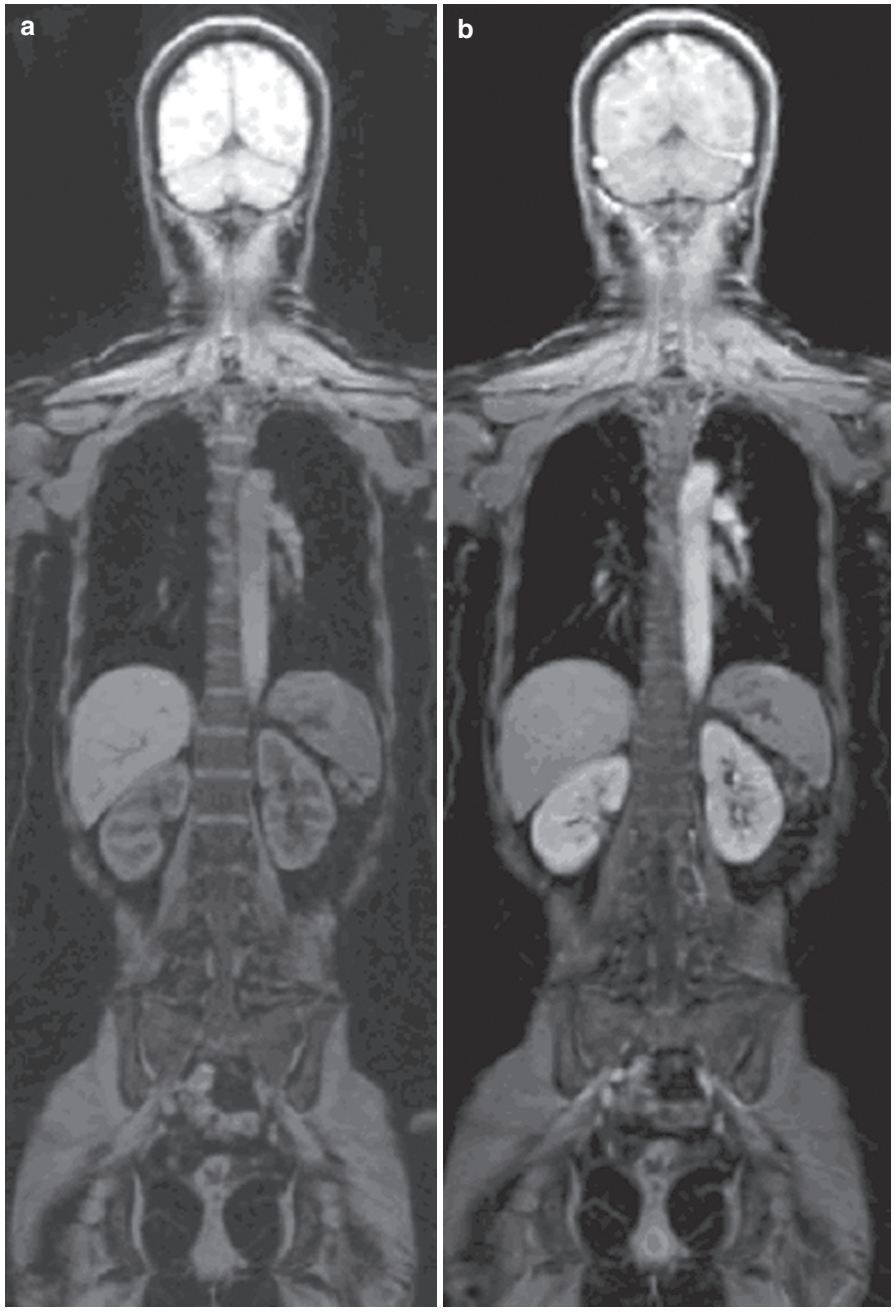

Fig. 13.2. Coronal water-only images derived using a 2-point DIXON technique (**a**) before and (**b**) after intravenous gadolinium-DTPA contrast administration. Such images can be rapidly acquired in breath-hold to provide good radiological contrast for the assessment of bones and soft tissues in the body

For qualitative assessment, a single high *b*-value (e.g. 600–1,000 s/mm^2) may suffice. The choice of the higher *b*-value may in part be limited by the scanner capability, which determines the image quality and signal-to-noise ratio. Generally, using a higher *b*-value would result in better background signal suppression, optimal for detecting tissues with reduced water diffusivity. Sometimes, the quality of DW-MR images of the lower thoracic and lumbar spine may be poor as a result of respiratory motion. If this occurs, it has been shown that the application of navigator-tracked respiratory-triggered DW-MRI can significantly improve the image quality (Spuentrup et al. 2003). For quantitative ADC calculations, three or more *b*-values would provide a more accurate fit of DW-MRI data, resulting in a more precise ADC estimate. Imaging using different *b*-values and the evaluation of quantitative ADC data were discussed in Chaps. 1–3.

In the appendicular skeleton, it is possible to apply alternative image acquisition schemes for DW-MRI. In one report (Oner et al. 2007), the application of a non-Carr-Purcell-Meiboom-Gill, single-shot, fast spin-echo sequence was found to result in images with a higher contrast-to-noise ratio compared with EPI technique. In the spine, it has also been shown that a steady-state free precession (SSFP) technique can be used for the assessment of vertebral pathologies (Baur et al. 2001a, b, 2002a, b; Raya et al. 2006) by visual and semi-quantitative analysis of the measured signal intensities. However, ADC quantification using the SSFP technique is much more challenging.

13.4.2.2 Diffusion-Weighted Whole-Body Imaging with Background Signal Suppression (DWIBS)

For whole-body imaging, DW-MRI is performed using single-shot STIR-EPI sequences (TR 6243/TE 59/TI 180 ms) using *b*-values of 0 and 600–1,000 s/mm^2. Thin image partition of 4–5 mm is typically used, with 1 mm of overlap. Images are acquired axially during free breathing and are performed at multiple imaging stations from the neck down to at least the pelvis. Where a receiver coil with a large field is available and if the patient is not too large or tall, imaging coverage may be achieved in just two stations on some MR imaging systems. Otherwise, imaging at four to five anatomical stations may be necessary, depending on the extent of coverage desired. Employing an imaging field of view (FOV) of 450 mm at each imaging station and an imaging matrix of 112 × 112, imaging at each station can be achieved in approximately 5 min.

Once the images are acquired, radial maximum intensity projections (MIPs) of the inverted grey-scale high *b*-value images may be processed and viewed on a workstation (see Chap. 14).

13.5 DW-MRI for the Detection and Characterization of Bone Involvement in Cancer

13.5.1 Normal Appearance of Bones on DW-MRI

Optimal interpretation of DW-MRI relies on knowledge of the normal appearances of bones on imaging. It must be remembered that bones are dynamic tissues that consist of a mineralized structure in which non-mineralized mesenchymal, haematopoietic and other connective tissue elements are distributed. In young adults, haematopoietically active red marrow is found predominantly in the pelvis and in the proximal long bones (Vande Berg et al. 1998). However, with increasing age, red marrow tissue is progressively replaced by fat, such that macroscopically it appears yellow in colour and is therefore known as "yellow marrow". In adults, about 50% marrow tissue is yellow marrow and this is predominantly located in the appendicular skeleton. The remaining 50% consists of red marrow found mainly within the axial skeletal and proximal long bones. In the elderly, the proportion of yellow marrow can further increase. Yellow marrow is composed of 95% fat cells, whereas red marrow is composed of 60% haematopoietic cells and 40% fat cells (Vande Berg et al. 1998). Using MR imaging, the marrow elements of bony tissues are well demonstrated. On T1-weighted imaging, red marrow appears intermediate signal intensity compared with the high signal intensity of yellow marrow. One useful fact to remember is that the pattern of distribution of red marrow in the body tends to be symmetrical across vertebrae and from one side of the body to the other (Daffner et al. 1986; Weinreb 1990; Vande Berg et al. 1998), a feature which may help to distinguish red marrow from disease infiltration.

Not surprisingly, there is considerable variation in the appearances of the bones and bone marrow on DW-MRI although the full range of imaging findings has not been fully documented. However, it is clear that the appearances of bones on DW-MRI vary with age as a result of fatty involution, and the DW-MRI appearance alters in tandem with the imaging findings on T1-weighted and STIR imaging. Fatty yellow marrow shows high signal intensity on T1-weighted imaging, and signal attenuation on high *b*-value DW-MRI because of the fat-suppression pulse that is applied with the EPI diffusion-weighted measurement. The limited mobility of protons associated with fat also means that normal yellow marrow returns lower ADC values compared with hypercellular or disease-infiltrated bone marrow (Nonomura et al. 2001). However, nulling of the fat signal by fat suppression may result in greater errors in the calculated ADC of normal bone marrow, because of the diminished accuracy of measuring signal attenuation from protons associated with the fatty tissues.

Regional variations in ADC values of normal bone marrow in non-oncological adult patients aged

between 28 and 82 years have been reported (Zhang et al. 2008). It was found that the mean ADC value of lumber vertebral bodies (0.62×10^{-3} mm^2/s) was significantly higher than that measured from the left ilium (0.40×10^{-3} mm^2/s) or the left femur (0.36×10^{-3} mm^2/s), reflecting the greater degree of fatty involution in the long bones and pelvis of adults (Zhang et al. 2008). In addition, osteoporosis which may result in increased fat deposition in bones has been found to be associated with a decrease in bone ADC values (Yeung et al. 2004). However, in another study, no relationship was found between the ADC values of vertebral bodies and the bone density determined by dual X-ray absorptiometry (Griffith et al. 2006).

On DWIBS imaging, the normal fat-replaced bone marrow is signal-suppressed on the high *b*-value images (Baur et al. 2001a, b). From the discussion above, it would be clear that in younger patients with haematopoietically active red marrow, the distribution of red marrow can be observed using DWIBS as these relatively cellular areas would be reflected in a high signal intensity. As in Fig.13.3 residual red marrow in the metaphyses of long bones in the younger individual demonstrate higher signal intensity compared with the bone marrow findings in the older man.

13.5.2 DW-MRI Detection of Metastatic Bone Disease

There are emerging studies demonstrating the value of DW-MRI for the detection of metastatic disease compared with conventional MR imaging and radionuclide studies (Nakanishi et al. 2005; Komori et al. 2007; Lichy et al. 2007; Moon et al. 2007; Nakanishi et al. 2007; Nemeth et al. 2007; Luboldt et al. 2008; Ohno et al. 2008; Takano et al. 2008; Xu et al. 2008; Laurent et al. 2009). In one of the largest studies to date, Ohno et al. (2008) evaluated 203 patients with non-small-cell lung cancers. Forty patients were found to have stage IV disease of which 11 had metastases only to bones. Interestingly, the addition of DW-MRI to conventional T1-weighted and STIR imaging resulted in a similar diagnostic accuracy and inter-observer agreement compared with ^{18}FDG-PET–CT (Ohno et al. 2008). Using DW-MRI alone was significantly less accurate on a per-patient and per-lesion basis compared with ^{18}FDG-PET–CT alone or the combination of DW-MRI with T1-weighted and STIR imaging. In another study, it was shown that DW-MRI was equal, if not superior to STIR and T1-weighted SE sequences, but as effective as ^{11}C-choline PET-CT for the detection of bone metastases in patients with prostate cancer (Luboldt et al.

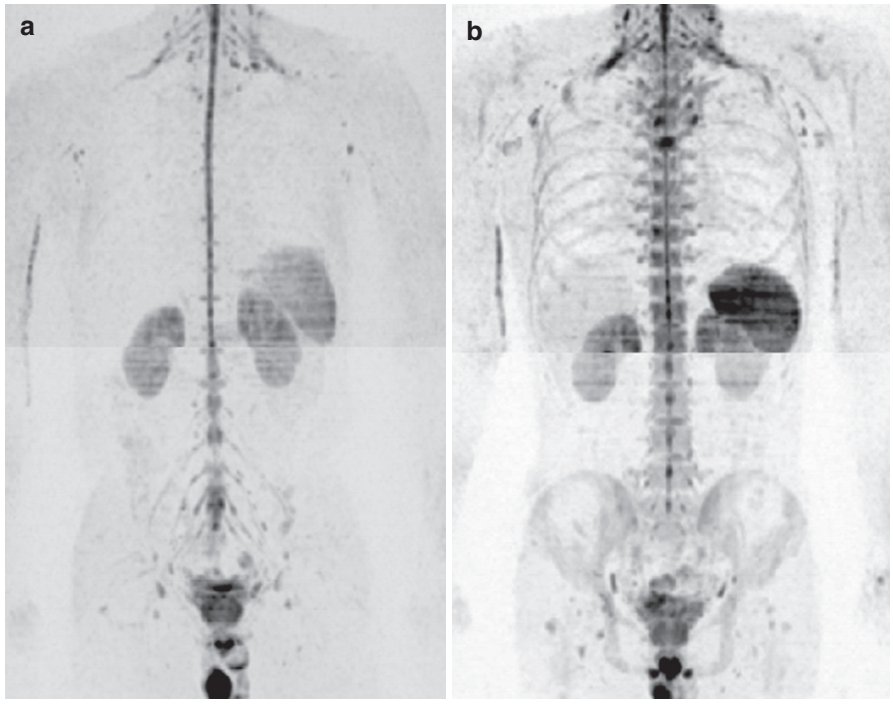

Fig. 13.3. Normal findings on DWIBS using a STIR EPI DW-MRI technique in (**a**) a 45-year-old man and (**b**) a 35-year-old man. These DW-MR images at a *b*-value of 600 s/mm^2 are displayed using an inverted grey scale. Note that in the older man (**a**), the signal intensity of the normal bone marrow is suppressed, although the spinal cord, nerve roots, kidneys, spleen and testes return low signal intensity on the inverted grey-scale images. However, in the younger man (**b**), there is relatively more signal returned from the red marrow within the bones especially in the axial skeleton

2008). Initial experience in 35 patients with metastatic melanoma showed that DWIBS was superior to ^{18}FDG-PET–CT for the detection of metastatic disease including bones (Laurent et al. 2009).

In our experience, we have assessed the diagnostic value of DW-MRI for detecting bony metastasis compared with conventional whole-body MR imaging and bone scintigraphy (Nakanishi et al. 2007). We found that the mean sensitivity and positive predictive value (PPV) of the combination DW-MRI with conventional MR imaging were 96% and 98%, respectively, which were superior to conventional MR sequences alone (88% and 98%) or bone scintigraphy alone (96% and 94%). Based on current evidence, DW-MRI and DWIBS appear to be highly promising for detecting metastatic disease to the bone, but the technique should be combined with conventional imaging for the best diagnosis to be made. An example of DWIBS in a patient with multiple bone metastases from prostate cancer is shown in Fig.13.4. The MIP images show the metastatic rib lesions clearly, which in this case, also correlate well with the bone scintigram appearance.

One of the key reasons why conventional imaging should not be ignored is because osteoblastic metastases may be missed on DW-MRI. Osteoblastic metastases may arise from prostate, breast, medulloblastoma, neuroendocrine and gastric cancers. Dense osteoblastic lesions often appear dark on the high *b*-value DW-MR images and may be difficult to distinguish from the signal suppressed fatty marrow (Fig. 13.5) (Hacklander et al. 2006). Osteoblastic metastases are better visualized on T1-weighted imaging, the corresponding CT imaging or by their increased tracer uptake on bone scintigraphy.

The advantages of DW-MRI over bone scintigraphy include the fact that osteolytic bone lesions may not be tracer-avid and hence may not be visible on scintigraphy (Fig. 13.6). Moreover, DW-MRI is useful for depicting lesions in the anterior ilium which may be less well seen on bone scintigraphy due to the position of the lesion in relation to the isotope camera (Fig. 13.7). There is a limit to the metabolic dimension of lesions that can be confidently detected using bone scintigraphy or ^{18}FDG-PET–CT. Bone lesions measuring less than 1 cm in diameter may be missed if they are not intensely tracer-avid. In our experience, small lesions measuring 1 cm or less are frequently better visualized on DW-MRI. In addition, DW-MRI or DWIBS may help to detect

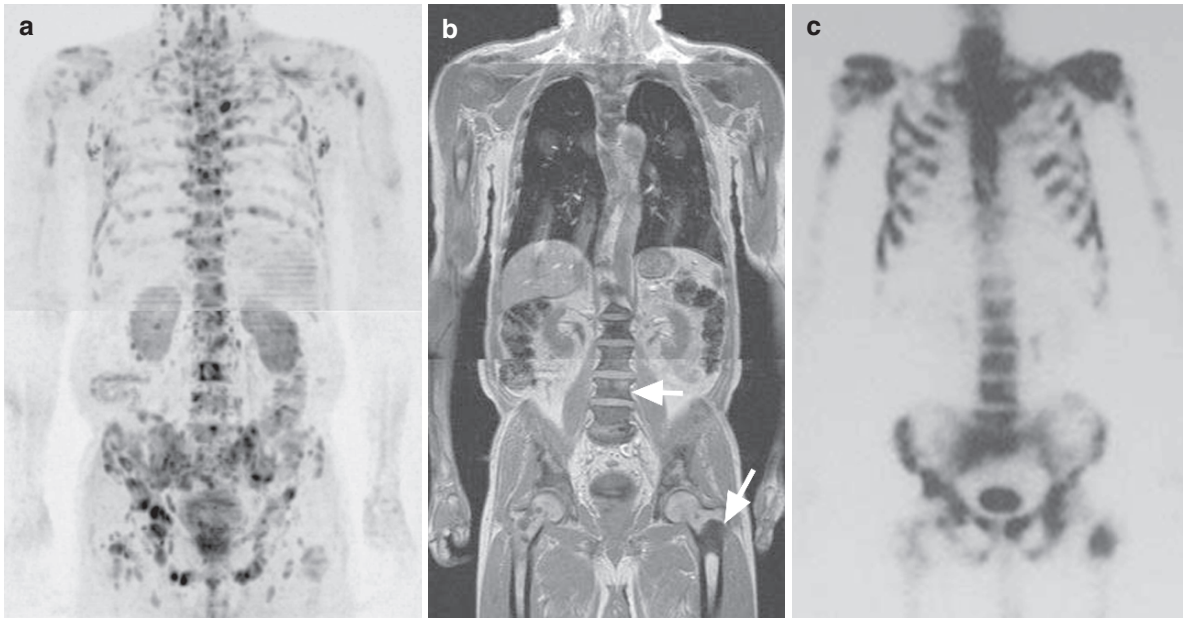

Fig. 13.4. Images of a 69-year-old man with multiple bone metastases from prostate carcinoma. (**a**) Maximum intensity projection of the inverted grey-scale $b = 600\,s/mm^2$ image shows multiple metastases in the bones depicted as low intensity lesions. (**b**) An image section from the whole-body T1-weighted acquisition shows very low intensity foci along the spine and within the left proximal femur, suggestive of osteoblastic metastases (*arrows*). (**c**) Bone scintigraphy confirms increased tracer uptake within the metastases. In this case, note the correspondence of imaging findings between DW-MRI, T1-weighted imaging and bone scintigraphy

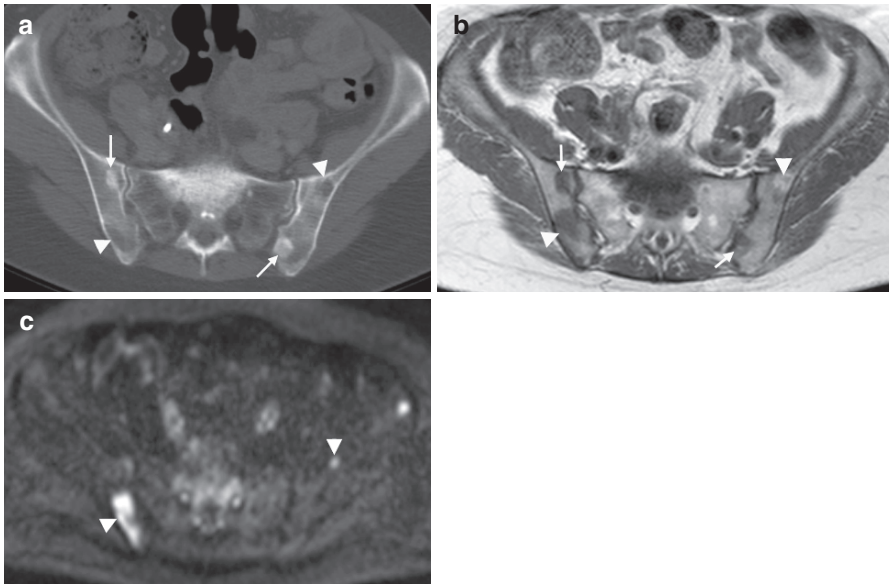

Fig. 13.5. Axial images of a 56-year-old woman with metastatic breast cancer. (**a**) CT imaging of the pelvis shows sclerotic (*arrows*) and lytic (*arrowheads*) bone metastases. (**b**) The sclerotic metastases return low signal intensity on T1-weighted imaging (*arrows*), although the lytic metastases (*arrowheads*) show more variable T1 signal intensity. (**c**) DW-MRI at b = 1,000 s/mm^2 demonstrates the high signal intensity from the lytic metastases (arrowheads) but the sclerotic bone metastases are signal-suppressed (Courtesy Dr. Koh, Royal Marsden Hospital, UK)

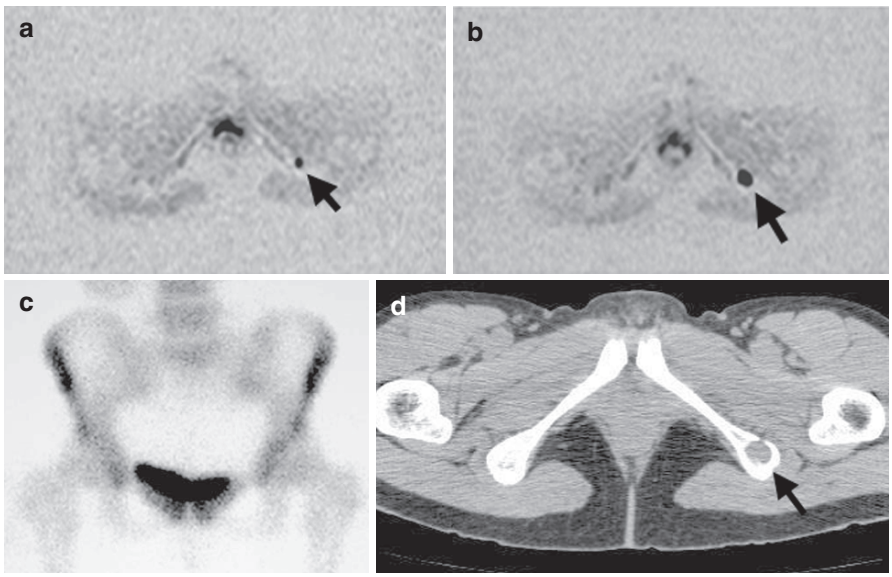

Fig. 13.6. Solitary metastatic lesion. Images of a 54-year-old woman with leiomyosarcoma of the uterus. (**a**) Focus of impeded diffusion in the left inferior pubic ramus (*arrow*) was missed on the initial reading of the inverted grey-scale DW-MR image at a b-value of 600 s/mm^2. (**b**) Repeat imaging 3 months later showed that the disease in the left pubic ramus has enlarged consistent with a metastasis (*arrow*). (**c**) The lesion was not visible on bone scintigraphy (**d**) CT imaging revealed an osteolytic lesion corresponding to the DW-MRI abnormality associated with cortical destruction (*arrow*)

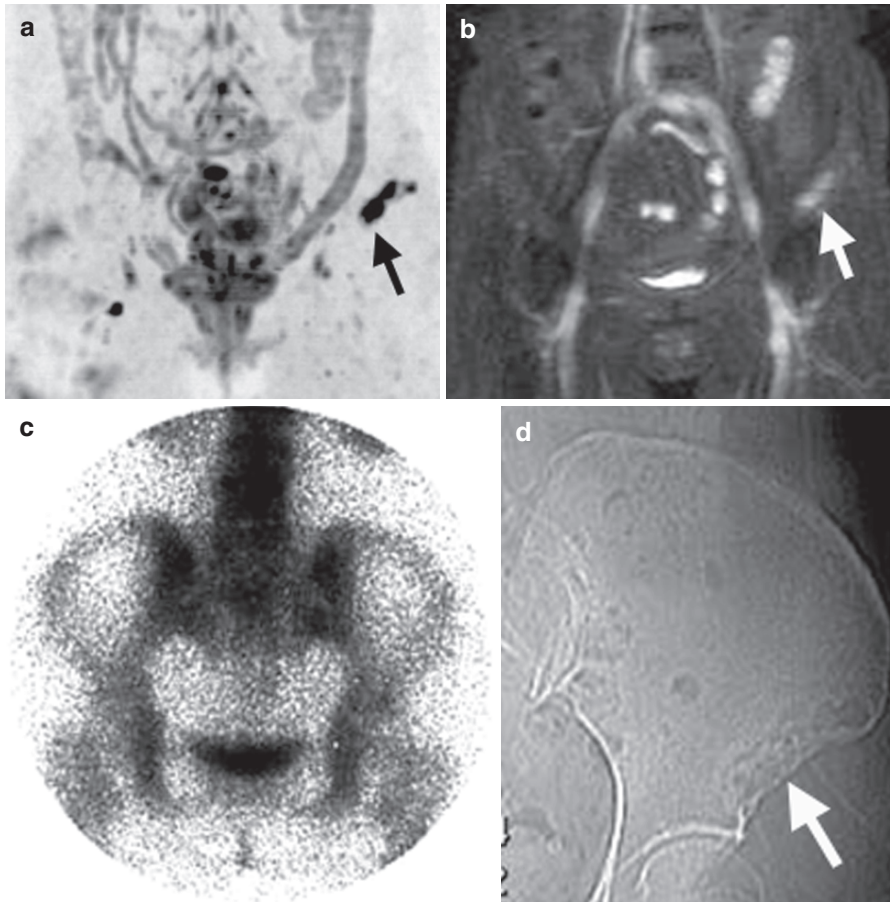

Fig. 13.7. Solitary metastasis. Images of a 68-year-old woman with breast carcinoma. (**a**) On the $b = 600\,s/mm^2$ inverted grey-scale coronal maximum intensity projection image, an area of decreased signal intensity is seen within the left ilium (*arrow*). (**b**) The corresponding area appears bright on the short-tau inversion recovery fat-suppressed image (*arrow*). (**c**) However, no significant tracer uptake was observed on bone scintigraphy. (d) Radiography reveals lucency and irregularity in the left ilium (*arrow*) which corroborate with the diagnosis of bone metastasis

unsuspected sites of extra-skeletal disease, such as in the lungs, breast, liver or lymph nodes (Fig. 13.8).

13.5.3 DW-MRI for Distinguishing Between Benign and Malignant Causes of Vertebral Collapse

Bone metastases in vertebral bodies occur in up to 10% of patients with primary neoplasms. A common result of such metastases is the collapse or fracture of the vertebral body. In oncological patients, it is often challenging to distinguish between a benign and a malignant vertebral body fracture. It has been estimated that up to one-third of vertebral fractures in patients with known malignancies are benign (FORNASIER et al. 1978). Differentiating benign from malignant causes of a vertebral fracture is important because different therapeutic management is undertaken for each.

Using conventional MR imaging and CT, it is frequently difficult – if not impossible – to determine whether a collapsed vertebral body is the result of a metastatic or benign process. A few radiological signs have been proposed to be helpful in this regard. Bauer et al. (2002a, b) described the "fluid sign" on MR imaging which was more frequently observed in benign osteoporotic fractures (40%) compared with malignant vertebral fractures (6%). This sign was observed as high signal intensity fluid on STIR imaging, often in a linear configuration adjacent to vertebral endplates (Baur et al. 2002a, b) and associated with high signal changes reflecting marrow oedema within the collapsed vertebral body. Another sign which was first observed on CT imaging in benign vertebral body fractures was the intravertebral "vacuum sign", which referred to linear gas densities within the vertebral body (Bhalla et al. 1998). This phenomenon can be observed in approximately 10% of osteoporotic fractures (Pappou et al. 2008). A study in 180 patients with radiological–pathological comparison showed a strong correlation between osteonecrosis and presence of the vacuum sign. The vacuum sign was found to have 85% sensitivity, 99%

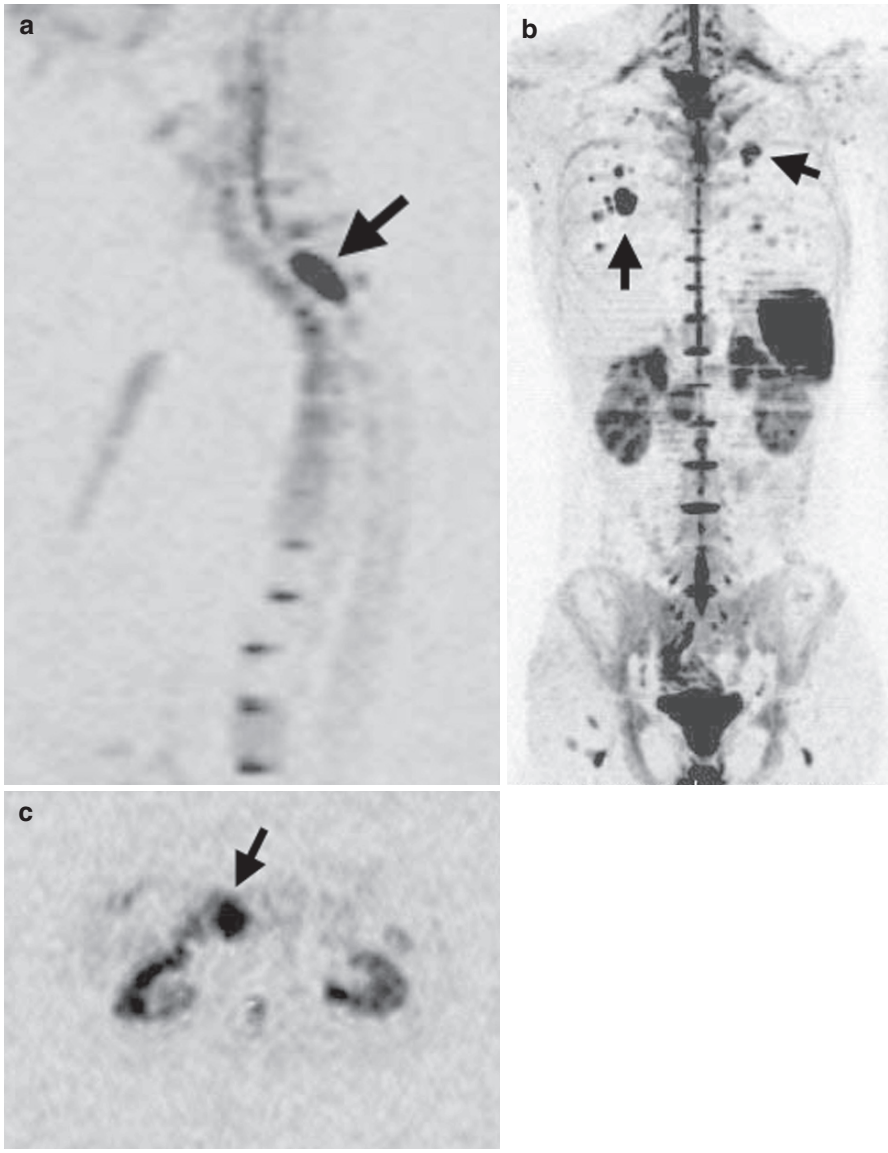

Fig. 13.8. DW-MR images of a 34-year-old man with an alveolar soft part sarcoma (ASPS) with spinal and pulmonary metastases. (**a**) On the sagittal reformat of the DW-MR images at a *b*-value of 600 s/mm^2, there is a low signal intensity metastasis arising from posterior elements of the lower cervical spine (*arrow*). (**b**) The coronal maximum intensity projection DW-MR image (inverted grey scale) shows numerous low intensity metastases within the lungs (*arrows*). (**c**) Axial DW-MR image through the upper abdomen reveals a mass inseparable from the head of the pancreas, consistent with a further site of metastasis

specificity and 91% positive predictive value for vertebral osteonecrosis (Libicher et al. 2007).

In 1998, Bauer et al. (1998) showed the feasibility of using the signal intensity of vertebral collapse on DW-MRI to discriminate between benign and malignant fractures. It was observed that malignant fractures were hyperintense compared with normal vertebrae (Fig. 13.9), but benign fractures appeared hypointense or isointense to normal vertebrae on DW-MRI (Fig. 13.10). This difference in MR appearance was ascribed to impeded water diffusion in the hypercellular tumour. However, in a subsequent study, Castillo et al. (2000) reported high signal intensity in both benign and malignant vertebral fractures. However, in that study, a relatively low *b*-value (b = 165 s/mm^2) was employed making the measurements sensitive to T2-shine-through effects. Further work by Baur et al. found that by increasing the diffusion-weighting of their SSFP imaging sequence it was possible to reduce the incidence of false-positive hyperintense osteoporotic fractures (Baur et al. 2001a, b) and later achieved a high sensitivity and specificity for the diagnosis of malignant vertebral fractures (Baur et al. 2002a, b). Another study also independently showed the utility of signal suppression on DW-MRI as a basis for discriminating benign

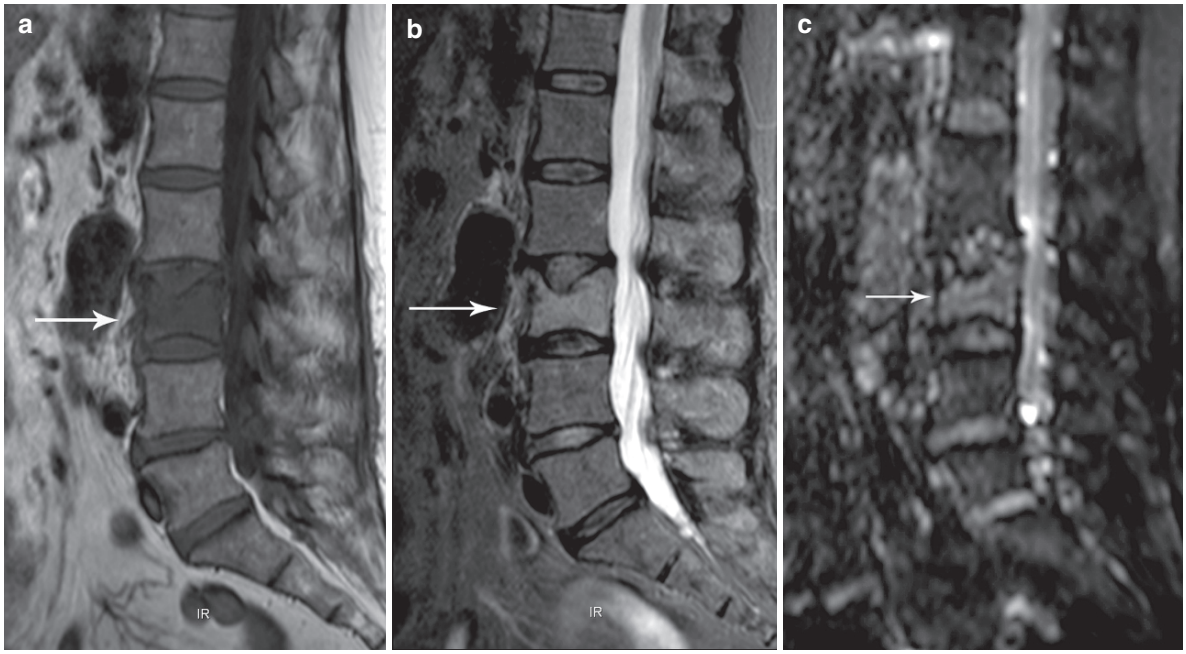

Fig. 13.9. Malignant vertebral fracture. An elderly man with metastatic disease to L3 vertebral body. (**a**) T1-weighted MR imaging demonstrates hypointensity within the L3 vertebral body (*arrow*) with loss of vertebral height. (**b**) The vertebral body appears mildly hyperintense on short-tau inversion recovery imaging (*arrow*). (**c**) Sagittal reformat of DW-MR image at a *b*-value of 1,000 s/mm^2 shows impeded diffusion within the verterbral body (*arrow*) consistent with malignant disease

from malignant vertebral fractures (Spuentrup et al. 2001).

As the measured signal intensity on DW-MRI is influenced by tissue diffusivity and T2-relaxation time, other authors have suggested that the ADC calculation may be a more robust method to discriminate between benign and malignant vertebral fractures. A summary of these findings is presented in Table 13.1. A few important points can be suggested from these observations:

1. There was substantial variation in the reported ADC values of benign and malignant vertebral lesions which reflected differences in the MR techniques applied and the choice of *b*-values.
2. The ADC values of normal bone marrow varied widely between studies. This could reflect physiological differences between studies, but could also be accounted for by measurement errors as a result of SNR variations, the choice of *b*-values or as a consequence of applying fat suppression to quantify diffusivity of fat-containing tissues. Nevertheless, the ADC of normal bone marrow appears to be relatively low in many of the recently published studies (Chan et al. 2002; Maeda et al. 2003; Griffith et al. 2006).
3. Malignant vertebral fracture or malignant marrow infiltration returned lower ADC values compared with benign vertebral fractures. However, the optimal ADC threshold value to apply to determine benignity has not been established. This is likely to vary with the imaging technique, as well as the number and choice of *b*-values applied for the DW-MRI study.
4. Infectious spondylosis resulted in low ADC values that were indistinguishable from those of malignant vertebral involvement. Hence, ADC values may not be appropriate for differentiating between malignant and infective conditions.

Despite these cautionary notes, in a well-conducted DW-MRI study performed using a wide range of *b*-values, a hypointense signal observed within a fractured vertebra on high DW-MRI at high *b*-values in combination with an increased ADC would be suggestive of a benign lesion.

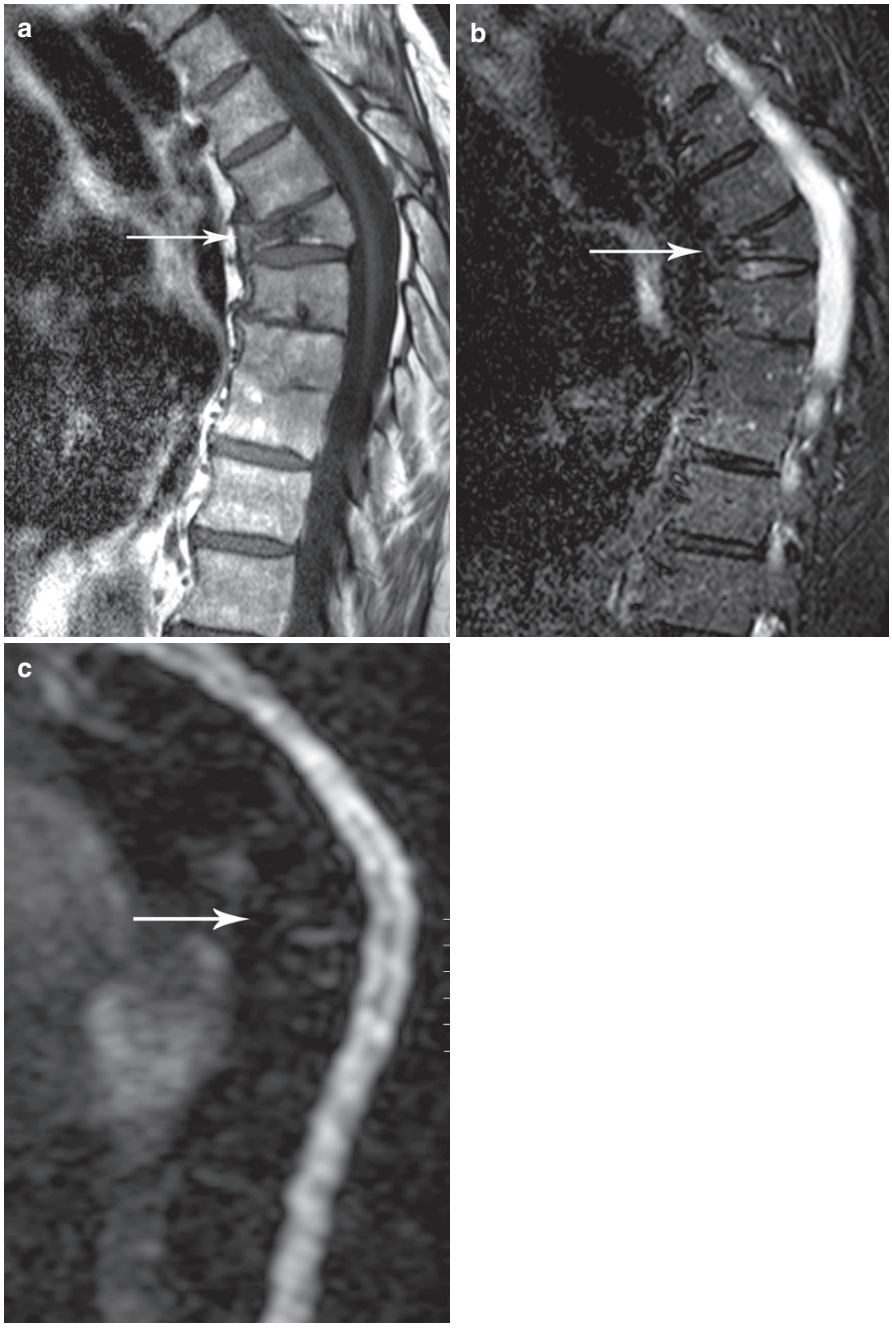

Fig. 13.10. Benign vertebral fracture. A middle-aged man with benign vertebral body fracture at T8. (**a**) T1-weighted MR imaging demonstrates hypointensity within the T8 vertebral body (*arrow*) associated with anterior wedging of the vertebral body. (**b**) The vertebral body appears isointense to other vertebral bodies on short-tau inversion recovery imaging (*arrow*). (**c**) Sagittal reformat of DW-MR images at a *b*-value of 1,000 s/mm^2 showed no abnormal increased signal intensity within the verterbral body (*arrow*) consistent with a benign process

13.5.4 DW-MRI for the Evaluation of Marrow Involvement by Haematological Malignancies

DW-MRI has also been used to demonstrate sites of marrow infiltration in haematological malignancies. For example, DW-MRI has been used to identify areas of marrow infiltration by leukaemia (Ballon et al. 2000). Although there have been reports detailing the improved diagnostic efficacy of whole-body MR imaging using conventional MR techniques for the assessment of patient with multiple myeloma (Mulligan et al. 2007; Lichy et al. 2008; Dinter et al. 2009), the role of DW-MRI for the assessment of disease in patients with multiple myeloma has not been established. However, based on our personal

Table 13.1. ADCs of normal vertebrae, benign fracture and malignant vertebral involvement reported in the published literature

	Imaging studies						
	(Herneth et al. 2000)	(Chan et al. 2002)	(Herneth et al. 2002)	(Zhou et al. 2002)	(Maeda et al. 2003)	(Griffith et al. 2006)	(Balliu et al. 2009)
Number of patients	5	32	22	27	64	110	45
Imaging technique	Navigator triggered EPI	Single-shot EPI	Navigator triggered EPI	Single-shot EPI	Line scan DW-MRI	Single-shot EPI	Single-shot EPI
b-Values (s/mm^2)	440, 880	200, 500, 800, 1,000	440, 880	0, 150, 250	5, 1,000	0. 100, 200, 300, 400, 500	0. 500
Mean ADC values ($\times 10^{-3}$ mm^2/s) ± standard deviation							
Normal vertebrae	1.3 ± 0.23	0.23 ± 0.05	1.66 ± 0.38	0.3–0.7	0.18 ± 0.09	0.43 ± 0.12	
Malignant fracture*/ infiltration**	0.39 ± 0.11**	0.82 ± 0.20*	0.71 ± 0.27* 0.69 ± 0.24**	0.19 ± 0.03*	0.92 ± 0.2* 0.83 ± 0.17**		0.9 ± 1.3**
Benign fracture		1.94 ± 0.35	1.61 ± 0.37	0.32 ± 0.05	1.21 ± 0.17		1.9 ± 0.39 (benign oedema)
Others		0.98 ± 0.21 (tuberculous spondylitis)					0.96 ± 0.49 (infectious spondylitis)

experience, it would appear that DW-MRI is also a potentially useful technique for evaluating the degree of marrow involvement by the disease. In an example of a patient with multiple myeloma (Fig. 13.11), DWIBS was used to highlight the anatomical distribution of bone disease in the body. The technique could also prove helpful in elucidating sites of extraosseous soft-tissue disease in patients with haematological malignancies.

13.6 Assessment of Treatment Response in Malignant Bone Disease

Assessment of the extent of response to treatment, during and after a specific therapy is crucial in clinical evaluation of cancer therapeutics. To unify the criteria of tumour response, the Response Evaluation Criteria in Solid Tumours (RECIST) were introduced in 2000, which were recently updated in version 1.1 (Eisenhauer et al. 2009). Although bone is a common site for metastatic disease, no consensus has been reached regarding the assessment of treatment response although several suggestions have been made (Bauerle et al. 2009).

In the original RECIST criteria, bone involvement was not considered to be a site of measurable disease. However, in the recently revised RECIST guidelines (version 1.1) (Eisenhauer et al. 2009), osteolytic lesions or mixed osteolytic/osteoblastic lesions with identifiable soft tissue components are now considered measurable by CT and MR imaging. Osteoblastic lesions, however, are still deemed immeasurable. Furthermore, bone scintigraphy, conventional radiographs and ^{18}FDG-PET cannot be used to quantify response, although these techniques may be applied to confirm the presence or resolution of lesions. However, size measurement provides a crude index of lesional response to therapy because successful treatment may not reduce lesion size. Hence, size measurement of bone metastases could potentially be confusing as it may not represent true disease response after a specific oncological therapy.

As an alternative to size measurement, Hamaoka et al. (2004) suggested that morphological changes to the appearance of bone metastasis on imaging may be

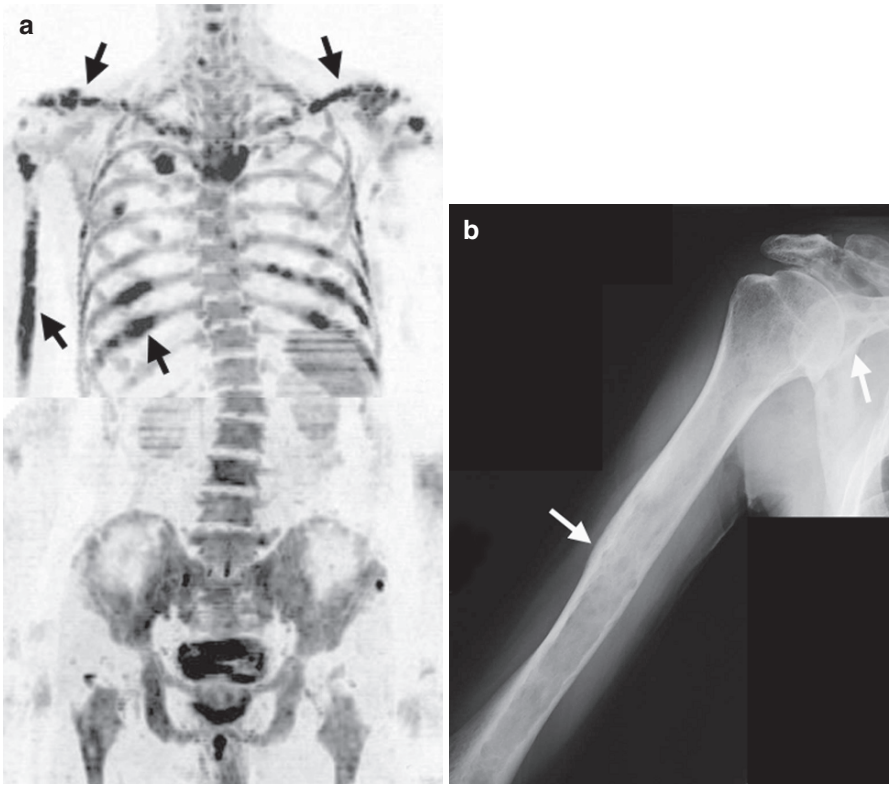

Fig. 13.11. Multiple myeloma. Images of a 69-year-old man with multiple myeloma with metallic internal fixator in the left humerus. (**a**) Inverted grey-scale coronal maximum intensity projection of the DW-MR image at a *b*-value of 600 s/mm^2 shows multiple low-intensity areas in the ribs, right humerus (*arrow*) and shoulder girdle (*arrows*). (**b**) Radiograph of the right humerus reveals multiple osteolytic (punched out) lesions along the humeral shaft scapula (*arrows*) and clavicle

used to gauge disease response. Using this approach, disease response was classified on the basis of disappearance of a lesion or the degree and pattern of calcifications (of an initially osteolytic lesion) after treatment. However, such classification is based on qualitative rather than quantitative assessment, and the criteria are not helpful for assessing osteoblastic disease, except when these lesions completely disappear after treatment.

13.6.1 DW-MRI for Assessing Treatment Response in Bone Malignancies

One of the perceived potentials of using DW-MRI to assess treatment response in bone disease is its ability to provide qualitative and quantitative assessment that reflects biological changes in the tumour following specific oncological therapy. Studies in small series have demonstrated increase in the ADC values within bone tumours and/or a decrease in the signal intensity on the high *b*-value DW-MR imaging following successful therapy (Byun et al. 2002; Hayashida et al. 2006a, b).

However, one of the challenges of performing quantitative DW-MRI for ADC measurements in the bone is the relatively poor SNR, which will impact on the reliability of the ADC measurements. Moreover, as bone tumours are often inhomogeneous, the mean ADC value will represent a mixture of elements representing different tissue types. Nevertheless, applying DW-MRI to quantify the ADC of malignant bone disease is feasible, particularly for circumscribed metastatic deposits associated with soft-tissue components. In such instances, DW-MRI measurements of the malignant disease could be made with good SNR and relatively free of artefacts. Early experience suggests that quantitative ADC values could be used to evaluate the response of malignant bone disease to treatment, and that ADC increases in tumours reflecting treatment response may be observed without any concomitant alterations on conventional morphological imaging (Fig. 13.12). Clearly, more studies are required to validate and demonstrate the efficacy of the technique in this clinical context.

One further development in using ADC to quantify disease response in bones is the application of the so-called functional diffusion map (Lee et al. 2007). Using this analysis method, ADC changes within the

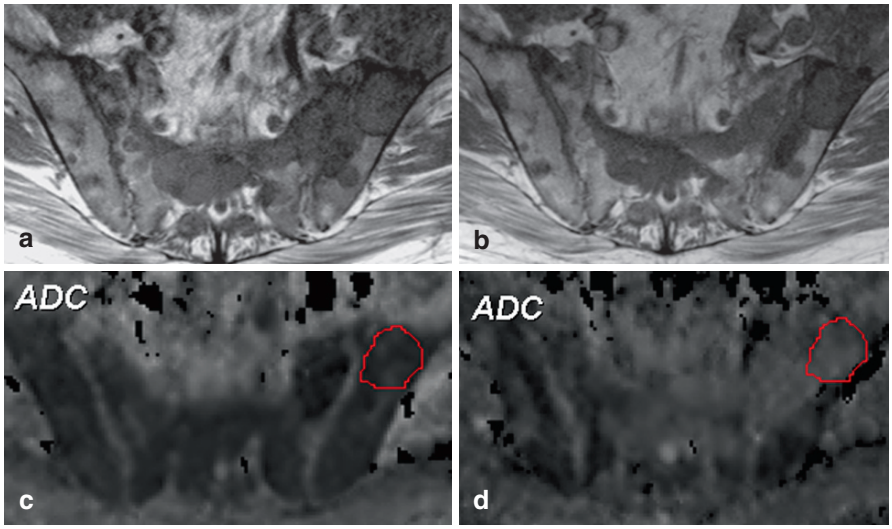

Fig. 13.12. Assessing treatment response of bone disease using DW-MRI. Images of a 72-year-old man with metastatic prostate cancer to bones. Axial T1-weighted imaging of the sacrum (**a**) before and (**b**) after treatment with novel drug (abiraterone) shows no significant difference in the imaging appearance at 28 days after treatment. However, the ADC maps of corresponding area (**c**) before and (**d**) after treatment shows clear increase in the mean ADC value (Pre = 0.69×10^{-3} mm^2/s and Post = 1.52×10^{-3} mm^2/s) within an area of disease (outlined in *red*) in the left ilium indicating drug treatment effects (Courtesy Dr. Koh, Royal Marsden Hospital, UK)

tumour are analysed on a voxel-by-voxel basis and the significance of ADC change is defined by the 5th and 95th percentiles of the pretreatment baseline voxel values. The number and percentage change in voxels above the 95th percentile or below the 5th percentile values after treatment are regarded as significant. Although research is still ongoing, the application of functional diffusion map analysis technique to define tumour response has been shown to correlate with disease survival in patients with cerebral gliomas (Hamstra et al. 2008) (see Chap. 10).

13.7 Benign Conditions That May Mimic Malignant Disease on DW-MRI

The high signal intensity observed on a high *b*-value DW-MR image is non-specific and may also result from benign conditions. This is because DW-MRI discriminates on the basis of cellularity, tissue viscosity and structure organization and not necessarily malignancy. For this reason, the readers should be acquainted with a range of benign bone conditions that may mimic malignant bone disease in patients with cancer. A few illustrative examples are presented below.

13.7.1 Osteoarthritis

Osteoarthritis typically occurs as a result of subchondral degeneration. On DW-MRI this condition is observed as mild hyperintensity on DW-MR images at lower *b*-values (e.g. 100 s/mm^2). However, as the *b*-value is increased to about 1,000 s/mm^2, the signal intensity from the degenerate area is usually diminished due to underlying cystic degeneration (Figs. 13.13).

13.7.2 Fracture

Bony fractures may be recognized on DW-MRI. Incidental fractures arising from the thoracic rib cage are not uncommon especially on DWIBS imaging (Fig. 13.14). However, it would be difficult to distinguish between a benign and malignant cause of the rib fracture based on the DW-MR image at a high *b*-value and ADC values alone.

13.7.3 Abscess

Figure 13.15 shows a tuberculous abscess in the soft tissue, which mimics a soft-tissue tumour. When

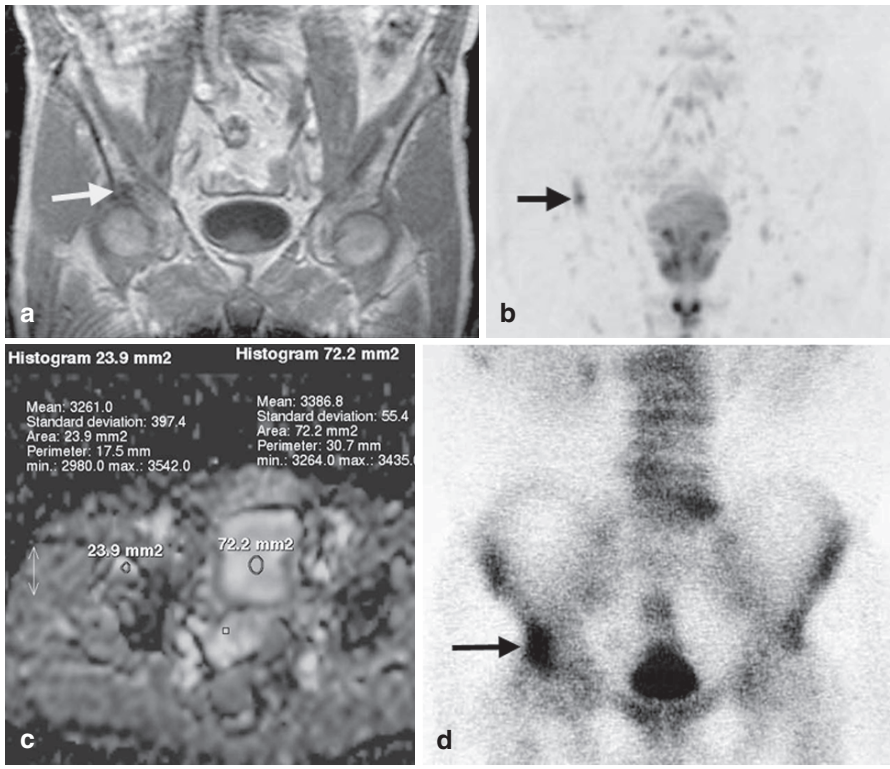

Fig. 13.13. Osteoarthritis. Images of a 69-year-old man with prostate cancer evaluated using whole-body conventional MR imaging and DWIBS techniques. (**a**) A low T1 signal intensity area was detected at the roof of the right acetabulum on T1-weighted coronal imaging (*arrow*). (**b**) This corresponded to an area of decreased signal intensity on the inverted grey-scale coronal maximum intensity projection DWIBS image (*arrow*). (**c**) The mean ADC value of the lesion was high (3.26×10^{-3} mm^2/s) and comparable to the ADC value of fluid in the urinary bladder, consistent with a subchondral cyst associated with osteoarthritis. (**d**) However, there was also relative increased tracer uptake in this area on bone scintigraphy, which raised the suspicion for metastasis. Subsequent follow-up imaging showed no confirmatory evidence of metastatic disease

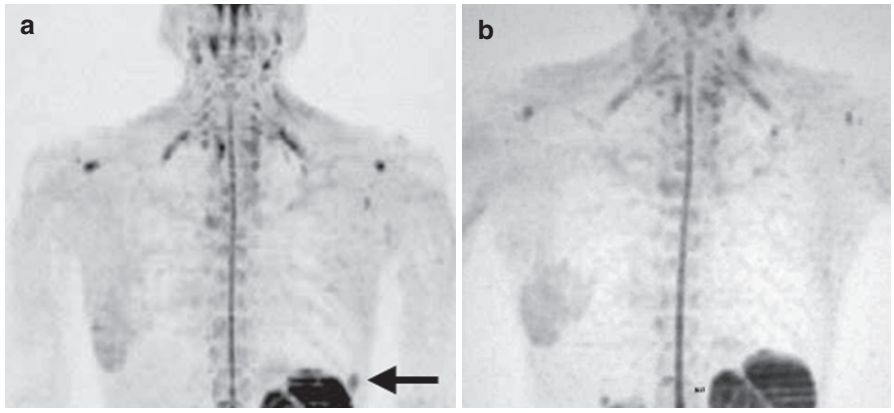

Fig. 13.14. Fracture. Cornonal DW-MR images of a 45-year-old woman with breast cancer who underwent whole-body MR imaging and DWIBS for detecting bone metastases. (**a**) On the inverted grey-scale maximum intensity projection DWIBS image of thorax, there was a solitary low signal intensity focus in the lower left rib (*arrow*). This was interpreted as a rib fracture. (**b**) Follow-up imaging 3 months later showed complete resolution of the abnormality

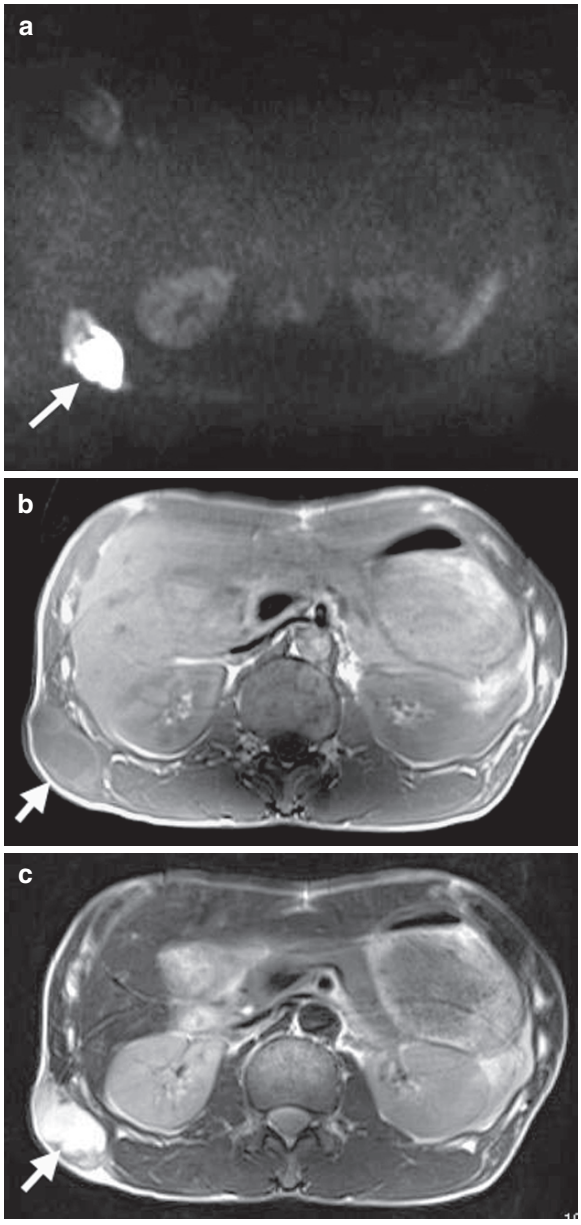

Fig. 13.15. Abscess. Images of a 48-year-old man with soft-tissue swelling in the right flank. (**a**) Axial DW-MR image at a *b*-value of 600 s/mm^2 showed a high signal intensity mass within the soft tissue of the right flank (*arrow*). (**b**) On T1-weighted imaging, the margins of the mass are mildly hyperintense, although the centre of the mass returns low signal intensity (arrow). (**c**) The mass returned inhomogeneous high signal intensity (*arrow*) on T2-weighted imaging. Pus was aspirated from the lesion and granulomatous inflammation confirmed

associated with bone changes, this appearance could be mistaken as metastatic soft-tissue disease. The composition of pus within an abscess is viscous and rich in protein, thus resulting in high signal intensity on the DW-MR images at high *b*-values and corresponding low ADC value.

13.7.4 Benign Tumour

Benign bone tumours also result in high signal intensity impeded water diffusion related to its underlying cellularity or structural organization (Hayashida et al. 2006a, b).

13.8 Conclusions

In conclusion, DW-MRI is a new imaging tool which can be used to detect and confirm malignant changes in the bones, as well as help distinguish benign from malignant conditions. However, DW-MRI should not be used as a stand-alone technique and should be combined with conventional and cross-sectional imaging techniques for the optimal assessment to be made. The technique is also promising for the assessment of therapeutic response in malignant bone diseases, which may prove useful for assessing the efficacy of therapies in the future.

References

Balliu E, Vilanova JC, Pelaez I, et al (2009) Diagnostic value of apparent diffusion coefficients to differentiate benign from malignant vertebral bone marrow lesions. Eur J Radiol 69:560–6

Ballon D, Dyke J, Schwartz LH, et al (2000) Bone marrow segmentation in leukemia using diffusion and T(2) weighted echo planar magnetic resonance imaging. NMR Biomed 13:321–8

Bauerle T, Semmler W (2009) Imaging response to systemic therapy for bone metastases. Eur Radiol 2009 May 26. [Epub ahead of print]

Baur-Melnyk A, Buhmann S, Becker C, et al (2008a) Whole-body MRI versus whole-body MDCT for staging of multiple myeloma. AJR Am J Roentgenol 190:1097–104

Baur-Melnyk A, Reiser M (2008b) Oncohaematologic disorders affecting the skeleton in the elderly. Radiol Clin North Am 46:785–98

Baur A, Huber A, Durr HR, et al (2002a) [Differentiation of benign osteoporotic and neoplastic vertebral compression fractures with a diffusion-weighted, steady-state free precession sequence]. Rofo Fortschr Geb Rontgenstr Neuen Bildgeb Verfahr 174:70–5

Baur A, Huber A, Ertl-Wagner B, et al (2001a) Diagnostic value of increased diffusion weighting of a steady-state free precession sequence for differentiating acute benign osteoporotic fractures from pathologic vertebral compression fractures. AJNR Am J Neuroradiol 22:366–72

Baur A, Stabler A, Arbogast S, et al (2002b) Acute osteoporotic and neoplastic vertebral compression fractures: fluid sign at MR imaging. Radiology 225:730–5

Baur A, Stabler A, Bruning R, et al (1998) Diffusion-weighted MR imaging of bone marrow: differentiation of benign versus pathologic compression fractures. Radiology 207: 349–56

Baur A, Stabler A, Huber A, et al (2001b) Diffusion-weighted magnetic resonance imaging of spinal bone marrow. Semin Musculoskelet Radiol 5:35–42

Bhalla S, Reinus WR (1998) The linear intravertebral vacuum: a sign of benign vertebral collapse. AJR Am J Roentgenol 170:1563–9

Byun WM, Shin SO, Chang Y, et al (2002) Diffusion-weighted MR imaging of metastatic disease of the spine: assessment of response to therapy. AJNR Am J Neuroradiol 23:906–12

Castillo M, Arbelaez A, Smith JK, et al (2000) Diffusion-weighted MR imaging offers no advantage over routine noncontrast MR imaging in the detection of vertebral metastases. AJNR Am J Neuroradiol 21:948–53

Chan JH, Peh WC, Tsui EY, et al (2002) Acute vertebral body compression fractures: discrimination between benign and malignant causes using apparent diffusion coefficients. Br J Radiol 75:207–14

Cheran SK, Herndon JE II, Patz EF Jr (2004) Comparison of whole-body FDG-PET to bone scan for detection of bone metastases in patients with a new diagnosis of lung cancer. Lung Cancer 44:317–25

Costelloe CM, Rohren EM, Madewell JE, et al (2009) Imaging bone metastases in breast cancer: techniques and recommendations for diagnosis. Lancet Oncol 10:606–14

Daffner RH, Lupetin AR, Dash N, et al (1986) MRI in the detection of malignant infiltration of bone marrow. AJR Am J Roentgenol 146:353–8

Dinter DJ, Neff WK, Klaus J, et al (2009) Comparison of whole-body MR imaging and conventional X-ray examination in patients with multiple myeloma and implications for therapy. Ann Hematol 88:457–64

Eisenhauer EA, Therasse P, Bogaerts J, et al (2009) New response evaluation criteria in solid tumours: revised RECIST guideline (version 1.1). Eur J Cancer 45:228–47

Eustace S, Tello R, DeCarvalho V, et al (1997) A comparison of whole-body turboSTIR MR imaging and planar 99mTc-methylene diphosphonate scintigraphy in the examination of patients with suspected skeletal metastases. AJR Am J Roentgenol 169:1655–61

Fornasier VL, Czitrom AA (1978) Collapsed vertebrae: a review of 659 autopsies. Clin Orthop Relat Res (131):261–5

Griffith JF, Yeung DK, Antonio GE, et al (2006) Vertebral marrow fat content and diffusion and perfusion indexes in women with varying bone density: MR evaluation. Radiology 241:831–8

Guo Y, Cai YQ, Cai ZL, et al (2002) Differentiation of clinically benign and malignant breast lesions using diffusion-weighted imaging. J Magn Reson Imaging 16:172–8

Hacklander T, Scharwachter C, Golz R, et al (2006) [Value of diffusion-weighted imaging for diagnosing vertebral metastases due to prostate cancer in comparison to other primary tumors]. Rofo 178:416–24

Hamaoka T, Madewell JE, Podoloff DA, et al (2004) Bone imaging in metastatic breast cancer. J Clin Oncol 22:2942–53

Hamstra DA, Galban CJ, Meyer CR, et al (2008) Functional diffusion map as an early imaging biomarker for high-grade glioma: correlation with conventional radiologic response and overall survival. J Clin Oncol 26:3387–94

Hayashida Y, Hirai T, Yakushiji T, et al (2006a) Evaluation of diffusion-weighted imaging for the differential diagnosis of poorly contrast-enhanced and T2-prolonged bone masses: initial experience. J Magn Reson Imaging 23:377–82

Hayashida Y, Yakushiji T, Awai K, et al (2006b) Monitoring therapeutic responses of primary bone tumors by diffusion-weighted image: initial results. Eur Radiol 16:2637–43

Herneth AM, Naude J, Philipp M, et al (2000) [The value of diffusion-weighted MRT in assessing the bone marrow changes in vertebral metastases]. Radiologe 40:731–6

Herneth AM, Philipp MO, Naude J, et al (2002) Vertebral metastases: assessment with apparent diffusion coefficient. Radiology 225:889–94

Hricak H, Choyke PL, Eberhardt SC, et al (2007) Imaging prostate cancer: a multidisciplinary perspective. Radiology 243:28–53

Huisman TA (2003) Diffusion-weighted imaging: basic concepts and application in cerebral stroke and head trauma. Eur Radiol 13:2283–97

Ichikawa T, Araki T (1999) Fast magnetic resonance imaging of liver. Eur J Radiol 29:186–210

Imamura F, Kuriyama K, Seto T, et al (2000) Detection of bone marrow metastases of small cell lung cancer with magnetic resonance imaging: early diagnosis before destruction of osseous structure and implications for staging. Lung Cancer 27:189–97

Jacobsson H, Goransson H (1991) Radiological detection of bone and bone marrow metastases. Med Oncol Tumor Pharmacother 8:253–60

Komori T, Narabayashi I, Matsumura K, et al (2007) 2-[Fluorine-18]-fluoro-2-deoxy-D-glucose positron emission tomography/computed tomography versus whole-body diffusion-weighted MRI for detection of malignant lesions: initial experience. Ann Nucl Med 21:209–15

Laurent V, Trausch G, Bruot O, et al (2009) Comparative study of two whole-body imaging techniques in the case of melanoma metastases: advantages of multi-contrast MRI examination including a diffusion-weighted sequence in comparison with PET-CT. Eur J Radiol 2009 Jun 2. [Epub ahead of print]

Lecouvet F (1998) Morphologic and quantitative MRI assessment of bone marrow in multiple myeloma and chronic lymphocytic leukemia: clinical and prognostic value. J Belge Radiol 81:301

Lee KC, Bradley DA, Hussain M, et al (2007) A feasibility study evaluating the functional diffusion map as a predictive imaging biomarker for detection of treatment response in a patient with metastatic prostate cancer to the bone. Neoplasia 9:1003–11

Libicher M, Appelt A, Berger I, et al (2007) The intravertebral vacuum phenomen as specific sign of osteonecrosis in vertebral compression fractures: results from a radiological and histological study. Eur Radiol 17:2248–52

Lichy MP, Aschoff P, Plathow C, et al (2007) Tumor detection by diffusion-weighted MRI and ADC-mapping–initial clinical

experiences in comparison to PET-CT. Invest Radiol 42: 605–13
Lichy MP, Mueller-Horvat C, Jellus V, et al (2008) Image quality improvement of composed whole-spine MR images by applying a modified homomorphic filter–first results in cases of multiple myeloma. Eur Radiol 18:2274–82
Luboldt W, Kufer R, Blumstein N, et al (2008) Prostate carcinoma: diffusion-weighted imaging as potential alternative to conventional MR and 11C-choline PET/CT for detection of bone metastases. Radiology 249:1017–25
Maeda M, Sakuma H, Maier SE, et al (2003) Quantitative assessment of diffusion abnormalities in benign and malignant vertebral compression fractures by line scan diffusion-weighted imaging. AJR Am J Roentgenol 181:1203–9
Mahner S, Schirrmacher S, Brenner W, et al (2008) Comparison between positron emission tomography using 2-[fluorine-18] fluoro-2-deoxy-D-glucose, conventional imaging and computed tomography for staging of breast cancer. Ann Oncol 19:1249–54
Miller TT (2008) Bone tumors and tumorlike conditions: analysis with conventional radiography. Radiology 246:662–74
Moon WJ, Lee MH, Chung EC (2007) Diffusion-weighted imaging with sensitivity encoding (SENSE) for detecting cranial bone marrow metastases: comparison with T1-weighted images. Korean J Radiol 8:185–91
Mulligan ME, Badros AZ (2007) PET/CT and MR imaging in myeloma. Skeletal Radiol 36:5–16
Nakanishi K, Kobayashi M, Nakaguchi K, et al (2007) Whole-body MRI for detecting metastatic bone tumor: diagnostic value of diffusion-weighted images. Magn Reson Med Sci 6:147–55
Nakanishi K, Kobayashi M, Takahashi S, et al (2005) Whole body MRI for detecting metastatic bone tumor: comparison with bone scintigrams. Magn Reson Med Sci 4:11–7
Nemeth AJ, Henson JW, Mullins ME, et al (2007) Improved detection of skull metastasis with diffusion-weighted MR imaging. AJNR Am J Neuroradiol 28:1088–92
Nonomura Y, Yasumoto M, Yoshimura R, et al (2001) Relationship between bone marrow cellularity and apparent diffusion coefficient. J Magn Reson Imaging 13:757–60
Ohno Y, Koyama H, Onishi Y, et al (2008) Non-small cell lung cancer: whole-body MR examination for M-stage assessment–utility for whole-body diffusion-weighted imaging compared with integrated FDG PET/CT. Radiology 248: 643–54
Oner AY, Aggunlu L, Akpek S, et al (2007) Diffusion-weighted imaging of the appendicular skeleton with a non-Carr-Purcell-Meiboom-Gill single-shot fast spin-echo sequence. AJR Am J Roentgenol 189:1494–501
Pappou IP, Papadopoulos EC, Swanson AN, et al (2008) Osteoporotic vertebral fractures and collapse with intravertebral vacuum sign (Kummel's disease). Orthopedics 31:61–6
Raya JG, Dietrich O, Reiser MF, et al (2006) Methods and applications of diffusion imaging of vertebral bone marrow. J Magn Reson Imaging 24:1207–20
Rubens RD (1998) Bone metastases–the clinical problem. Eur J Cancer 34:210–3
Schmidt GP, Reiser MF, Baur-Melnyk A (2009) Whole-body MRI for the staging and follow-up of patients with metastasis. Eur J Radiol 70:393–400
Spuentrup E, Buecker A, Adam G, et al (2001) Diffusion-weighted MR imaging for differentiation of benign fracture edema and tumor infiltration of the vertebral body. AJR Am J Roentgenol 176:351–8
Spuentrup E, Buecker A, Koelker C, et al (2003) Respiratory motion artifact suppression in diffusion-weighted MR imaging of the spine. Eur Radiol 13:330–6
Suarez SV, Amadon A, Giacomini E, et al (2009) Brain activation by short-term nicotine exposure in anesthetized wild-type and beta2-nicotinic receptors knockout mice: a BOLD fMRI study. Psychopharmacology (Berl) 202:599–610
Sugimoto E, Tamagawa M, Okawara K, et al (1988) [Radiologic detection of metastatic bone tumors]. Gan No Rinsho 34:1491–7
Takahara T, Imai Y, Yamashita T, et al (2004) Diffusion weighted whole body imaging with background body signal suppression (DWIBS): technical improvement using free breathing, STIR and high resolution 3D display. Radiat Med 22:275–82
Takano A, Oriuchi N, Tsushima Y, et al (2008) Detection of metastatic lesions from malignant pheochromocytoma and paraganglioma with diffusion-weighted magnetic resonance imaging: comparison with 18F-FDG positron emission tomography and 123I-MIBG scintigraphy. Ann Nucl Med 22:395–401
Thomson V, Pialat JB, Gay F, et al (2008) Whole-body MRI for metastases screening: a preliminary study using 3D VIBE sequences with automatic subtraction between noncontrast and contrast enhanced images. Am J Clin Oncol 31: 285–92
Vande Berg BC, Malghem J, Lecouvet FE, et al (1998) Magnetic resonance imaging of normal bone marrow. Eur Radiol 8:1327–34
Vanel D, Casadei R, Alberghini M, et al (2009) MR imaging of bone metastases and choice of sequence: spin echo, in-phase gradient echo, diffusion, and contrast medium. Semin Musculoskelet Radiol 13:97–103
Weinreb JC (1990) MR imaging of bone marrow: a map could help. Radiology 177:23–4
Winterbottom AP, Shaw AS (2009) Imaging patients with myeloma. Clin Radiol 64:1–11
Xu X, Ma L, Zhang JS, et al (2008) Feasibility of whole body diffusion weighted imaging in detecting bone metastasis on 3.0T MR scanner. Chin Med Sci J 23:151–7
Yasumoto M, Nonomura Y, Yoshimura R, et al (2002) MR detection of iliac bone marrow involvement by malignant lymphoma with various MR sequences including diffusion-weighted echo-planar imaging. Skeletal Radiol 31: 263–9
Yeung DK, Wong SY, Griffith JF, et al (2004) Bone marrow diffusion in osteoporosis: evaluation with quantitative MR diffusion imaging. J Magn Reson Imaging 19:222–8
Zhang CY, Rong R, Wang XY (2008) Age-related changes of bone marrow of normal adult man on diffusion weighted imaging. Chin Med Sci J 23:162–5
Zhou XJ, Leeds NE, McKinnon GC, et al (2002) Characterization of benign and metastatic vertebral compression fractures with quantitative diffusion MR imaging. AJNR Am J Neuroradiol 23:165–70